Author(s): Makhlouf, Jawher; Louis, Hitler; Benjamin, Innocent; Ukwenya, Elizabeth; Valkonen, Arto; Smirani, Wajda

Title: Single crystal investigations, spectral analysis, DFT studies, antioxidants, and molecular docking investigations of novel hexaisothiocyanato chromate complex

Year: 2023

Version: acceptedVersion

Please cite the original version:

Makhlouf, J., Louis, H., Benjamin, I., Ukwenya, E., Valkonen, A., & Smirani, W. (2023). Single crystal investigations, spectral analysis, DFT studies, antioxidants, and molecular docking investigations of novel hexaisothiocyanato chromate complex. Journal of Molecular Structure, 1272, Article 134223. https://doi.org/10.1016/j.molstruc.2022.134223

Single crystal investigations, spectral analysis, DFT studies, antioxidants, and molecular docking investigations of novel hexaisothiocyanato chromate complex

Jawher Makhlouf [a], Hitler Louis [b], Innocent Benjamin [b], Elizabeth Ukwenya [b], Arto Valkonen [c] and Wajda Smirani [a*]

a- Labortory of Material Chemistry, Faculty of Sciences of Bizerte, University of Carthage, Bizerte Zarzouna, Tunisia

b- Computational and Bio-Simulation Research Group, University of Calabar, Calabar, Nigeria

c- Departement of Chemistry, University of Jyvaskyla, 40014 Jyvaskyla, Finland

[*]**Corresponding author:** wajda_sta@yahoo.fr

Abstract

We successfully synthesized 3D supramolecular structure of 2-Amino-6-methyl piridinium hexaisothiocyanatochromate (III) complex, $(C_6H_9N_2)_3\,[Cr(SCN)_6].H_2O$. The structure of the synthesized material was confirmed by single crystal X-ray crystallography, UV, FT-IR, photoluminescence, and thermal analysis. A detailed analysis of the intermolecular close interactions and their percentage contribution has been performed based on the Hirshfeld surfaces and their associated two-dimensional fingerprint plots as well as the other quantum chemical descriptors using density functional theory (DFT) computation were occurred in order to insight into the role of weak molecular interactions of the complex that influence the self-assembly process and crystal packing. In this context, the novel complex was characterized by various techniques, the FTIR analysis was registered to revel the vibrational modes of the compound, add to the study of the optical properties using a polar solvent to carry out the UV–visible analysis, and fluorescence to investigate the optical property along with the biological studies by the evaluation of anti-free radical activity. Thermal analyses were performed for this complex to account for the thermal decomposition of complex and to investigate the use of this complex as a single-source precursor for the synthesis of chrome sulfide (CrS) under Argon atmosphere and chrome

oxide (CrO) under air. Furthermore, molecular docking was performed on the synthesized complex docked with 4CIA to further understand the biological activities and applications as a potential cardiovascular disease drug candidate. On the other hand, the MESP was intrigued with the stability of the complex that was created between the receptor and the title chemical. According to the mulliken population analysis, the target molecule had an electric potential between -0.221 and 0.221. When compared to the typical medicine, the examined molecule showed extremely strong inhibitory potential in terms of the number of hydrogen bond interactions, according to the results of molecular docking. As a result, the head chemical may be used as a substitute medication candidate for the treatment of cardiovascular disease.

Keywords: *Transition metal, Inorganic chemistry, Optical properties, spectroscopy, Antioxidant property, DFT, Molecular docking, Biological activity.*

1.0 Introduction

Coordination compounds based on transition metal precursor and thiocyanates have become of increasing interest in the last few years. First of all, the thiocyanate anion is a versatile ligand that can coordinate to metal cations in different ways leading to compounds with a large structural variety [1-6], Chromium has been known as a micronutrient for mammals for decades, but progress in elucidating the role of chromium has proceeded slowly. However, recent studies have shed light on a potential role of chromium in maintaining proper carbohydrate and lipid metabolism at a molecular level, it is also an essential nutrient for normal function of the human body as it helps regulate how your body processes fats and sugars [7]. In our research work, we have obtained several isomeric or polymorphic modifications of the chromium that have special interest, due to the properties of these compounds which can directly be correlated with their structures as an example the ($HCrO_4$) used widely in electroplating and other industries and occurs naturally at high concentration in ultramafic rocks. Under oxidizing conditions, Cr is highly soluble and mobile as the Cr(VI) anions which is strongly adsorbed onto solid surfaces and less toxic [8]. For the preparation of such modifications, we frequently use a typical solid-state synthesis protocol, where the ligands are stepwise removed by thermal annealing. This procedure very often leads to the formation of metastable modifications but also to compounds with condensed thiocyanate networks that in most cases cannot be obtained from solution [9,10]. The synthesis of coordination compounds by solid state synthesis is nothing unusual and also other approaches are reported as the case of the Chromium-Diphenyl carbazide Reaction [11].The 2-amino, 6-methyl, pyridine is a

monodentate neutral N ligand system which show a high ability to donate towards a wide range of transition metal ions giving rise to very stable complexes [12-14], which has also an aromatic nitrogen atom which unshared electron pairs are excellently located to act together in binding to metal ions, is known as a good π-acceptor [15, 16] and has been extensively used as a ligand in both analytical and preparative coordination chemistry [17-19]. Additionally, virtual screening of the compound against promising target receptor (PDD: 4CI4) for the treatment of heart failure was performed to investigate the best binding receptors. This was achieved utilizing molecular docking**.** These methods are well known for identifying best binding molecules to receptors and discriminate between strong and weak binders.

The Hirshfeld surface analysis has been performed to completely characterize the intermolecular interactions and explain the crystalline architecture. In addition, the Cr complex was investigated by various spectroscopic studies. DFT calculations have been performed for the investigation of the interesting properties of the titled complex.

2.0 Methods

2.1 Experimental

2.1.1 Synthesis

The solid metal complex $(C_6H_9N_2)_3$ $[Cr(SCN)_6].H_2O$ was prepared by mixing solution of the organic ligand and $CrCl_2.3H_2O$, dissolved in a mixture of water and Ethanol then stirred together. The thiocynic salt KSCN was dissolved in water and was added dropwise to the well stirred green-cyan mixture. The obtained mixture was left to evaporate for a week at ambient temperature. The solid was filtered and finally stored.

2.1.2 Structural characterization

2.1.2.1 X-ray crystallography

In order to analyze the crystal structure of the obtained compound, an X ray automated four circle diffractometer (Bruker-Nonius Kappa CCD, diffractometer). Single crystal X ray diffraction measurement were carried out on an automated four circle diffractometer (Bruker-Nonius Kappa CCD, diffractometer), containing a monochromatized-mirror using a graphite-monochromated MoKα (λ= 0.71073 Å) as radiation at 170 K. The structure was solved and reined on F2 with the direct methods using the SHELXL software [20] incorporated in the wing X program package

[21]. A summary of Crystal data and experimental details are shown in **Table S1** of the supporting information**.**

2.1.2.2 In situ high-pressure XRPD experiments

The measurements were performed using a PANalytical X'Pert Pro MPD Reflection Powder diffraction System with **CuKα1** radiation (λ =1.540598 Å) equipped with a PIXcel semiconductor detector from PANanlytical. Moreover, the results obtained by Vezzalini method [22] and Ferro et al. [23] on the powdered sample compressed in silicone oil, showed a close agreement up to 5 GPa. Above 5 GPa, a contribution of deviatoric stress to the peak broadening of the powder diffraction patterns cannot be excluded. The quality of the silicone oil used for this study has been carefully tested in several previous HP experiments.

2.1.2.3 Infrared spectroscopy

Infrared measurement was performed at room temperature, using a Nicolet IR200 spectrometer, in the spectral range scans were run over the range 400-4000 cm^{-1}.

2.1.2.4 UV–Visible spectroscopy

UV measurement was performed at room temperature using a Perkin Elmer Lambda 35 spectrophotometer. Scans were run over the range 200-800 cm^{-1}.

2.1.2.5 The photoluminescence spectroscopy

The photoluminescence (PL) measurement was carried out, at room temperature, using the PerkinElmer LS55 fluorescence spectrometer equipped with a 450 W xenon lamp as the excitation source using solid sample at room temperature.

2.1.2.6 The thermal analyses

The thermal analysis spectra of were obtained with a simultaneous thermogravimetry-differential thermal analysis (TG-DTA) using PYRIS 1 TGA instrument (using 12.4 mg for a heating rate of 5 $K.min^{-1}$ for the titled compound in the temperature range 300-880 K under inert atmosphere (nitrogen gas).

2.2 Evaluation of anti-free radical activity

The scanning activity of the DPPH radical was measured according to the protocol described by Louli et al. **[24],** A solution of DPPH was prepared by dissolving 4 mg of DPPH in 90 ml of DMSO. The solution was then placed in the dark for three hours. In glass tubes, one prepares a series of dilutions of the extract as well as that of the positive control dichloromethane (DCM) with a concentration of the stock solution of (5 mg / 10 ml) in order to obtain the following concentrations (0, 2.5; 5; 8; 11; 13.85 µg / ml). After 5 ml of the DPPH solution are introduced. After shaking, the tubes are placed in the dark at room temperature for 30 minutes. Regarding the negative control, it contains only the DPPH solution and the ethanol with an equal volume of 2.5 ml. Reading is performed by measuring the absorbance at 515 nm using a UV / Vis spectrophotometer **[25]**. Antioxidant activity is estimated using equation (1).

$$(I\ \%) = [Abs\ control\ \_\ Abs\ sample / Abs\ control] \times 100 \quad (1)$$

where:

- (I %): percentage of anti-free radical activity.
- Abs sample: absorbance of the sample.
- Abs Control: absorbance of negative control.

2.3 Computational details

2.3.1 Density functional theory (DFT) details

The geometry optimization was carried out using B3LYP, PBE0 and ωB97XD/Gen level of theory employing the Gaussian 16 **[26]** with Gaussian-View 6.0.16 **[27]** software packages. The koopsman approximation which is associated with the frontier molecular orbital (FMO) were used to better understand the complex's reactivity and binding capabilities. Chemcraft was employed in this study to plot the HOMO-LUMO while GaussSum was used to explore the density of state spectrum. The computational method (PBE0/ 6-311++G(d,p) was utilized to achieve the molecular electrostatic potential (MESP) and the Mulliken population analysis for the purpose of elucidating sites susceptible to both electrophilic and nucleophilic attack. This was achieved utilizing the Multiwfn **[28]** function program package. The natural bond orbital (NBO) calculations were carried out to estimate the energy level, clearly illustrating the intra- and intermolecular interactions within the title compound. On the other hand, the intermolecular interactions, the

fingerprint plots of internal and external distances (di, de) were carried out using the Crystal Explorer 3.1 software **[29]** imported on a CIF file.

2.3.2 Molecular docking details and choice for selecting target receptors

To further investigate and assess the binding efficiency of our complex with the target protein 4CIA, linked to cardiovascular disorders were obtained from the protein data bank. Clopidogrel was the conventional drug employed in this study to serve as a control for the purpose of validating the title compound employed in this study. 4CIA is examined as a promising receptor for remediating diseases associated with cardiovascular tissues **[30]**. Computational docking, commonly referred to as molecular docking analysis, was carried out on the complex and the target protein using Auto Dock-Vina. Vina uses local optimization as well as a gradient optimization technique to automatically cluster the findings. After loading each of the three target proteins with inflammatory connections that were retrieved from the protein data bank, the file was saved in pdbqt format, the water molecules were removed, polar hydrogens were added, and the file was then saved in Bio-discovery Studio. After selecting the target proteins' active site residues, the grid box was made for the target protein using a 1 spacing. The molecule in PDB format was downloaded using the ligand option in Auto-Dock Tool, and all non-rotatable bonds were changed to rotatable. After that, the complex was stored in PDBQT format. Interestingly, haven evaluated the results obtained by electrostatic forces (number of hydrogen bond interactions), electrodynamics forces, and Steric forces in order to understand the interactions formed when atoms of various particles get close to one another and alter their reactivity.

3.0 Results and Discussion

3.1 X-ray diffraction study

$(C_6H_9N_2)_3$ $[Cr(SCN)_6].H_2O$ crystallizes in a triclinic system with the $P\bar{1}$ space group. The asymmetric unit comprises two hexa(isothiocyanate) Chrome $[Cr(NCS)_6]^{3-}$ anions, three 2-Amino-6-methylpiridinium cations and a water molecule (**Fig. 1**). Selected bond distances and angles are given in **Table S2** of the supporting information. For the $[Cr(NCS)_6]^{3-}$ anions, the coordination geometry of the central Cr(III) ions can be described as a slightly distorted octahedron (**fig. S1**). The average Cr-N bond distance is 1.995 (6) Å and the N– Cr–N bond angles vary in the range 180.0 (3) –89.7 (2) ° for the anion containing Cr1 as well as Cr2which are symmetric atoms.

These values are in agreement with those found in complexes containing the $[M(NCS)_6]^{3-}$ anion, such as $[Bu_4N]_3Gd(NCS)_6$ (Bu4N =tetra-n-butylammonium**) [31],** the $[(C_6H_5)_4P]_3In(NCS)_6$ **[32]** and the $[Bu_4N]_3Fe(NCS)_6$ **[33-37]. Fig. 2** shows that the $[Cr(NCS)_6]^{3-}$ anions are arranged along the c-axis direction. These anions lie at (0, 0, 0), (½, 0, 0) to form anionic layers parallel to the (b,c) plane (**Fig. 2**). The nearest Cr…Cr distance is 6.869 (5) Å. The solvent molecules establish intermolecular hydrogen-bonding interactions linking neighboring thiocyanate anions through O-H … S and N-H…S hydrogen bonds with lengths ranging respectively from 2.69 Å to 2.71 Å and from 2.50 Å to 2.71 Å, contributing to the $R_8^4(44)$ ring as shown in **Fig. 4(a).** Before discussing the hydrogen bond itself, the matter of hydrogen bond definitions must be addressed. This is an important point, because definitions of terms often limit entire fields. It is, also, a problematic point because very different hydrogen bond definitions have been made, and part of the literature relies quite uncritically on the validity (or the value) of the particular definition that is adhered to. Today, it is known that the hydrogen bond is a much broader phenomenon than sketched above. In fact, the phenomenon has continuous transition regions to such different effects as the covalent bond, the purely ionic, the cation - π, and the van der Waals interaction. The electrostatic dominance of the hydrogen bond is true only for some of the occurring configurations, whereas for others it is not. The H... A distance isn't shorter in all hydrogen bonds than the sum of the van der Waals radii. For the organic entities, it was found that the neighboring cations containing the N8, N8A and N8B, N8B atoms are grouped into dimers through weak interactions N8B—H8F···$O1^{vi}$ generated by the water molecules (**Fig. S2**). Therefore, hydrogen-bonding interactions play a major role in the stability of the compounds.

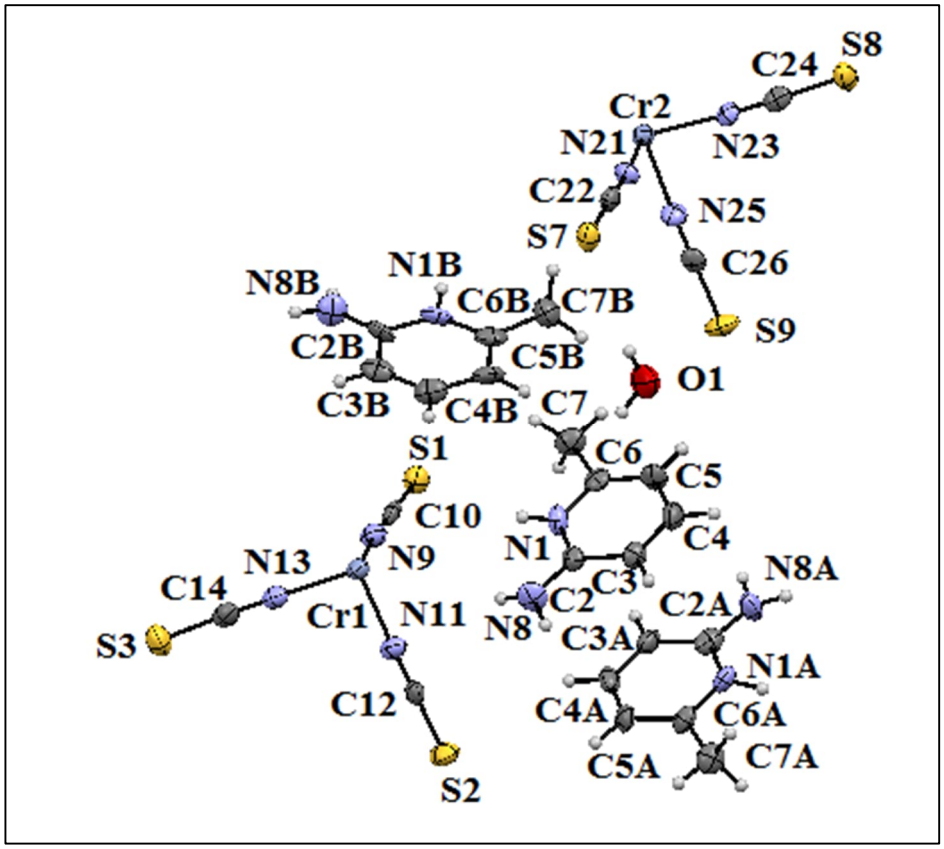

Fig. 1: ORTEP of $(C_6H_9N_2)_3\,[Cr(SCN)_6].H_2O$.

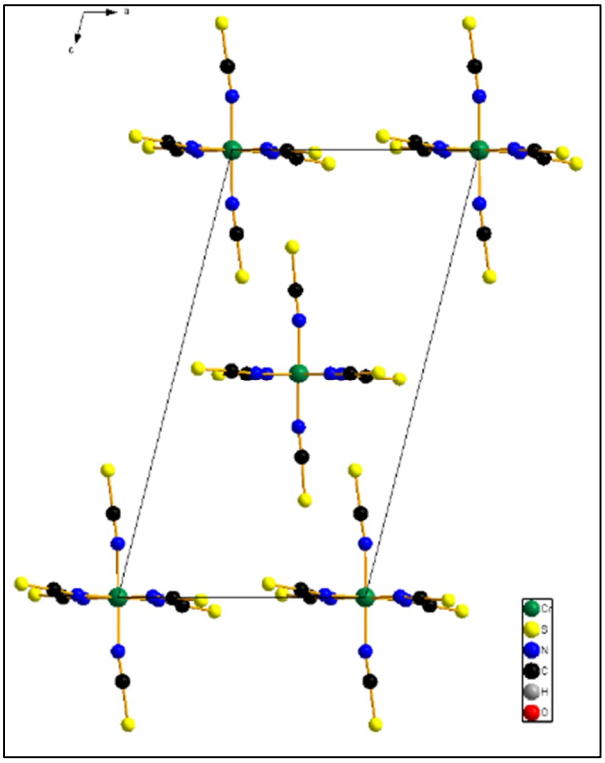

Fig. 2: Crystallographic showing the Cr(SCN)6 moieties forming a layer parallel to the (a,c) plane in $(C_6H_9N_2)_3\,[Cr(SCN)_6].H_2O$.

Fig. 3 shows N–H…S interactions between the cations and anions. Except for the **S2** atom, we notice that all S atoms of the $[Cr(NCS)_6]^{2-}$ anions are involved in H-bonding interactions. **S3 and S7** atoms are double acceptors, while each one **of S1, S3, S7, S8 and S9** sulfur atoms are involved in only one hydrogen bond. These weak interactions improve the stability of the network as presented in **table 1**. The discrete complex $(C_6H_9N_2)_3[Cr(SCN)_6].H_2O$ is linked by intermolecular **O–H···S** hydrogen bonds between the H atoms of the water molecules and the thiocyanate S atoms into layers parallel to the a/c plane (**Fig.3** and **Table 1**) add to the intermolecular **N–H···S** hydrogen bonds with between the H atoms of the N entity belongs to the cation molecules and the thiocyanate S atoms into layers parallel to the a/c plane (**Fig.3** and **Table 1**). These layers are further connected by intermolecular hydrogen bonding into a to three-dimensional network in the structure and contribute to the cohesion and stability of the compound. Regarding the donor-acceptor bond lengths, all the hydrogen bonds in the studied system are found to be weak (D—A

> 3 Å) and have an electrostatic interaction type **[38]** (**Fig.3**). It is noted that this topology of the thiocyanate network is quite rare and usually observed with the more M (III) anions such as $(C_6H_5NO_2)_3Fe(SCN)_6$ $(H_2O)_2$ **[39-40].** All these intermolecular hydrogen bonds give rise to three-dimensional network in the structure and contribute to the cohesion and stability of the compound. Regarding the donor-acceptor bond lengths, all the hydrogen bonds in the studied system are found to be weak (D—A > 3 Å) and have an electrostatic interaction type **[41].** The conformation of the coordination complex is determined by the relative magnitude of various interatomic interactions which can be stabilizing (hydrogen bond, complementary dipole, n-stacking) or destabilizing (van der Waals repulsion, dipolar repulsion). In recent times, the CH…π interactions has been identified as a weak, attractive, donor-acceptor type interaction between an acidic CH group and a basic π-system, which can affect the conformation of molecules and transition-state structure due to the short contacts between the phenyl ring atoms. In addition, the stability of the Cr complex is improved by the CH…π interactions between the CH frame and the aromatic rings with the distance 3.599 Å, add to the π-π stacking interaction between aromatic rings which adds more stability to the three-dimensional framework with the distance 3.910 Å (**fig.4(b)**).

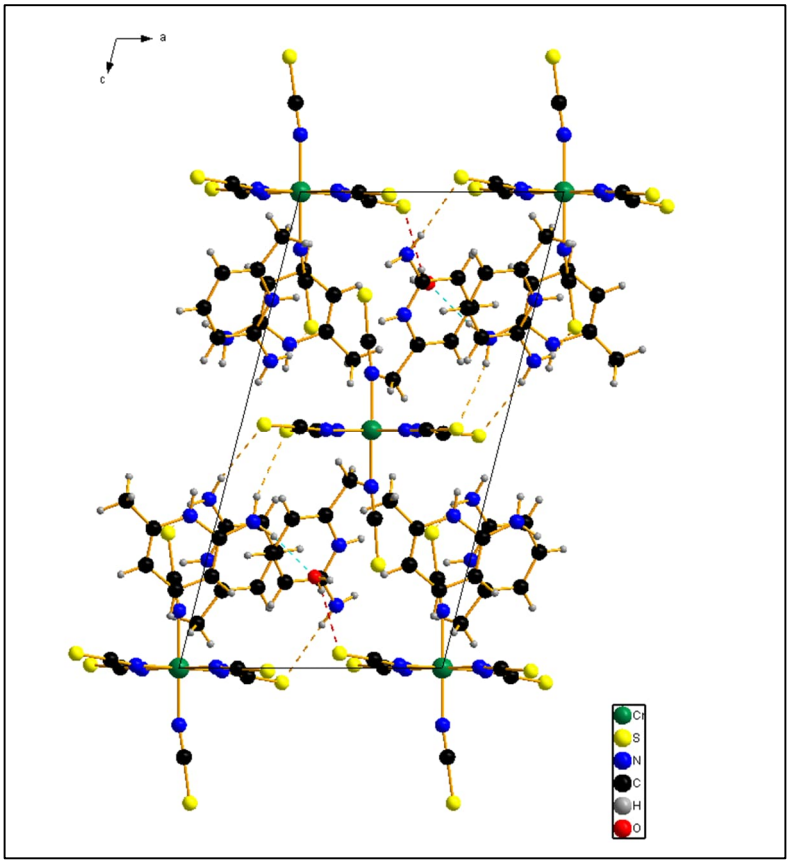

Fig. 3: Projection along the b-axis of the structure of $(C_6H_9N_2)_3\,[Cr(SCN)_6].H_2O$. Dotted lines indicate hydrogen bonds.

Table 1: Hydrogen-bond geometry (Å, °).

D—H···A	D—H	H···A	D···A	D—H···A
N1—H1···S1	0.88 (2)	2.50 (3)	3.325 (6)	158 (6)
N8—H8A···S3iii	0.88 (2)	2.52 (2)	3.395 (7)	176 (7)
N8—H8B···S7iv	0.88 (2)	2.71 (4)	3.495 (7)	150 (6)
N1A—H1A···S7v	0.88 (2)	2.43 (2)	3.301 (6)	175 (6)
N8A—H8C···S8iv	0.88 (1)	2.52 (2)	3.396 (7)	172 (7)
N8A—H8D···S1iii	0.92 (7)	2.53 (7)	3.373 (8)	153 (6)
N1B—H1B···S8ii	0.88 (2)	2.44 (3)	3.294 (6)	163 (6)
N8B—H8E···S9vi	0.90 (2)	2.65 (3)	3.511 (8)	162 (7)
N8B—H8F···O1vi	0.90 (2)	2.02 (3)	2.905 (10)	168 (7)
O1—H1O···S7	0.84 (2)	2.69 (2)	3.499 (7)	160 (6)
O1—H1P···S3i	0.86 (2)	2.72 (2)	3.538 (7)	159 (5)

Symmetry codes : (i) −x, −y+1, −z; (ii) −x+1, −y, −z+1; (iii) x+1, y, z; (iv) x, y+1, z; (v) x+1, y+1, z; (vi) x−1, y, z.

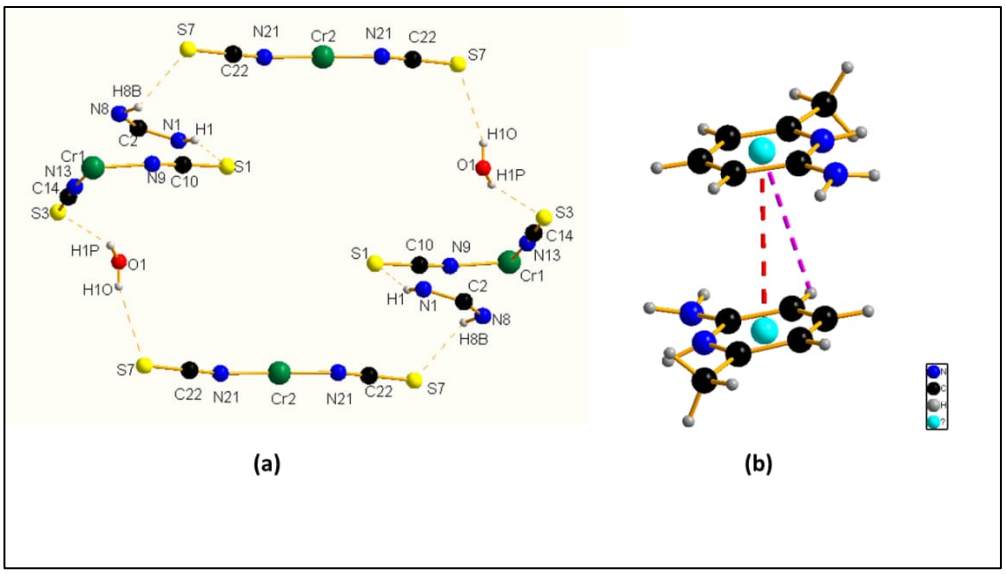

Fig. 4: (a) Hydrogen bonds ring of $(C_6H_9N_2)_3[Cr(SCN)_6].H_2O$. (b) CH-π and π-π interactions.

3.2 XRPD data analysis

The background curve was fitted by a Chebyshev polynomial with an average of 21 coefficients. A pseudo-Voigt profile function proposed by Thomson et al. **[42]** and cutoff of the peak intensity were applied. Above this pressure, due to the bad quality of the data, the structural model was kept fixed and only unit-cell parameters were refined. The isotropic thermal parameters of all atoms were not refined and kept to the reported values (**Fig. S3**). Structure determination of compound was performed by Rietveld refinements of the corresponding isostructural Cr complex. The profile function was described in both cases with the fundamental parameter approach **[43],** while the background was modelled by Chebychev polynomials of 12th and 11th order. The Rietveld refinement for the compound was carried out using a rigid body model for describing the ligand hmpy, whereas the individual bond lengths of the thiocyanate group were restrained. Moreover, hydrogen atoms were fixed at geometric calculated positions (**Fig. S1**) and an overall isotropic thermal displacement parameter was used for all atoms.

3.3 Hirshfeld surface and contacts enrichment ratio

The application of Hirshfeld surface **[44]** analysis occupies a huge interest within the field of crystallography. Hirshfeld surfaces and fingerprint plots **[45]** were generated and based on the crystallographic information file (CIF) using Crystal Explorer **[46-47].** Hirshfeld surfaces allow the visualization of intermolecular interactions. Colors and color intensities are related to the relative strength of the interaction and the short or long contacts. This technique is a powerful tool for visualizing and identifying interatomic compound interactions. It provides a virtual image where the different types of interactions are clearly identified by the shapes, outlines and colors provided by the calculation. The dnorm map analysis have graphically illustrated the relative positions of neighboring atoms belonging to molecules that interact with each other. The normalized contact distance (dnorm) was calculated via the equation (2).

$$Dnorm = \frac{di - r_i^{\mathrm{U}dw}}{r_i^{\mathrm{U}\mathrm{dw}}} + \frac{de - r_e^{\mathrm{U}\mathrm{dw}}}{r_e^{\mathrm{U}\mathrm{dw}}} \qquad (2)$$

is the van der Waals radius of the atom that lies inside the surface of Hirschfeld, while reUdw is the van der Waals radius of the atom that lies outside of the surface of Hirshfeld. The Hirshfeld surface of the title compound is illustrated in **Fig. 5**. In this latter a color gradient is used, which

varies from red (distances shorter than sum of UdW with negative dnorm value) through white (represents the contact around UdW separation with a dnorm value of zero) to blue (distance longer than of UdW with positive dnorm value).

The red spots over Hirshfeld surface point out the inter-contacts included in hydrogen bonds. It is well observed in **Fig. 5** that the red circular collapsing is attributed to N—H…S/ N—H…O/ O—H…S hydrogen-bonding interactions. In the dnorm map, the vivid red spots in the Hirshfeld surface are due to short normalized S—H distances corresponding to N— H···S interactions. Hydrogen-donor groups constitute the convex blue regions on the shape-index surface and hydrogen-acceptor groups appear in concave red regions. 3D graphics, Curvedness (**Fig. S4**) and Shape index (**Fig. S5**) are also used to identify the characteristic packaging modes existing in crystal. The small flat segments delimited by the blue outline observed on the Curvedness graph indicate the absence of (π ... π) interactions so that there is no evidence of the adjacent red and blue triangles on the surface of Shape index (**Fig. S5**). This result was confirmed by a structural X-ray analysis. The examination of the 2D fingerprints used to highlight the atoms participating in close contacts. In addition, the analysis of these footprints helped to reread numerical values to the surfaces previously described. The characteristic features in the 2D-fingerprint plots (**Fig. S6**) obtained from the Hirschfeld were further investigated in order to find out the directional interactions. This analysis shows the relative contribution of each contact present in the compound. In these plots **di** corresponds to the closest internal distance from a given point of the Hirschfeld, and **de** to the closest external contacts (i.e., external distance). The two-dimensional fingerprint plots quantify the contributions of each type of non-covalent interaction to the Hirshfeld surface. The major contribution with 32.1 % of the surface is due to S···H contacts, which represent van der waals interactions, followed by H···C, H···H, H···N, Cr···N, O ···H, S ···S ,N ···N and Cr···O interactions, which contribute 20.5, 16.1, 13.7, 3.7, 3.2, 2.2, 1.8 and 1.6% respectively, these contributions are observed as two sharp peaks in the plot of **Fig. S6.**

The percentage of contacts between one (X…X) or two (X…Y) chemical elements in a crystal packing is information given by CrystalExplorer which can be used to indirectly calculate the enrichment ratios **[48]**, the proportion of Hirshfeld surface contacts involving the (X,Y) pair of elements is referred to as CXY. The proportion Sx of chemical type X on the molecular surface is obtained by the summation [49]:

$$Sx = Cxx + \frac{1}{2} \Sigma CXY \qquad \textbf{(3)}$$

The value CXY includes both X…Y and Y…X contacts in the SX sum, where the first and second atoms are interior and exterior to the Hirshfeld surface. The factor $\frac{1}{2}$ relates to the fact that CXY contributes to both Sx and SY summations. The summation of all the surface proportions is equal to unity [**50**]:

$$\Sigma x\ Sx = 1 \qquad (4)$$

The ratio of random contacts R_{XY} between the two chemical elements X and Y is then introduced. The R_{XY} values are defined as if all contact types X…Y in the crystal packing were equi-distributed between all chemical types and are obtained by probability products [**51**].

$$R_{XX} = S_X S_X \quad \text{and} \quad R_{XY} = 2 S_X S_Y \qquad (5)$$

The enrichment ratios E_{XY} were computed for sets of molecules belonging to several classes of molecules and were analyzed as a function of S_X values. In order to limit the number of E_{XY} values and S_X variables present in the contacts data, compounds containing only two or three different chemical elements were selected and grouped in their respective set: C_{HH}, C_{HS}, C_{HC}, C_{HN}. Intermolecular interactions identified are assessed by an analysis of enrichment ratios (E_{XY}) which provide a quantitative measure of the probability of intermolecular interactions **[52]** that occur on the Hirshfeld Surface as shown in **table 2**. The contacts on Hirshfeld surfaces of the three independent organic cations were analyzed. The contacts types are very similar on the three molecules as the correlation coefficient between the Cxy values of two cations is between 0.918 and 0.994. The fingerprint plot of the contacts on only one cation was therefore computed. The contacts types between the layer of Cr(NCS)6 anions and the layer of organic cations add to water are shown in Table 4. It shows that the S…H-N strong hydrogen bonds, constitute the major of the interface (32.1%) and are enriched at E = 1.65, The N-H…O, weak hydrogen bond (3.2%) enriched at E = 0.12.

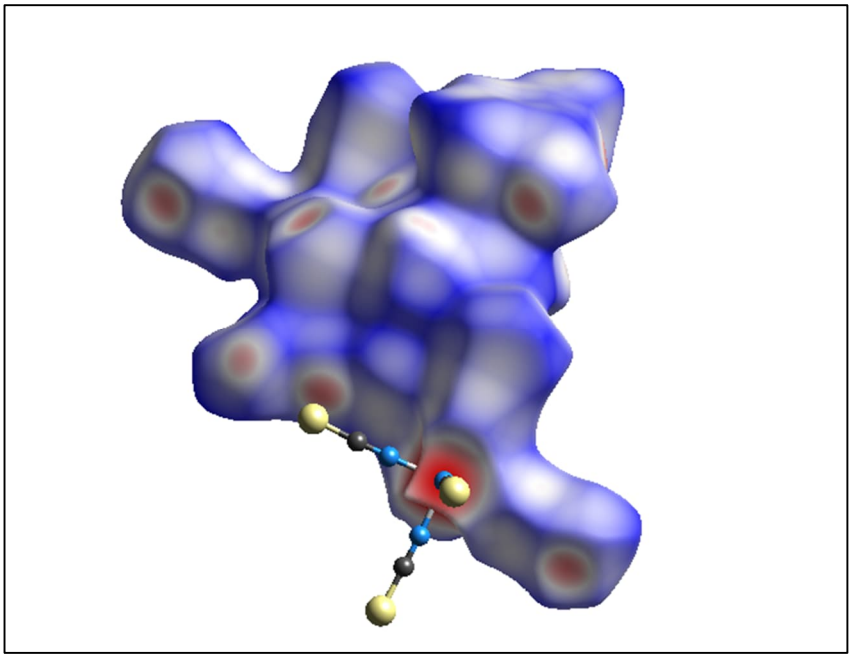

fig. 5: View of the dnorm quantity mapped on the Hirshfeld surface of the asymmetric unit of the title compound. The red color represents the area on the surfaces where the atoms make intermolecular contacts closer than the sum of their Van der Waals radii.

Table 2: Chemical proportions on the Hirshfeld surface, % contact types and their enrichment ratios.

% real contact : C_{XY}						
Atom	**H**	**C**	**N**	**O**	**Cr**	**S**
H	16.1%	20.5%	13.7%	3.2%	-	32.1%
C	20.5%	6 ,3%	-	-	-	-
N	13.7%	-	1.8%	-	3.7%	-
O	3.2%	-	-	-	1.6%	-
Cr	-	-	3.7%	1.6%	-	-
S	32.1%	-	-	-	-	2.3%
%surface	54,25	11,05	12.35	2.4	2.65	17.85
% Random contact: R_{XY}						
Atom	**H**	**C**	**N**	**O**	**Cr**	**S**
H	29,43%	11.98%	1.19%	1.30%	-	19.36%
C	11.98%	1.22%	-	-	-	-
N	1.19%	-	1.52%	-	0.65%	-
O	1.30%	-	-	-	0.12%	-
Cr	-	-	0.65%	0.12%	-	-
S	19.36%	-	-		-	3.18%
Enrichment ratios: E_{XY}						
Atom	**H**	**C**	**N**	**O**	**Cr**	**S**
H	0,54	1.71	11.51	2.46	-	1.65
C	1.71	5,16	-	-	-	-
N	12.24	-	1.18	-	5.69	-
O	2.46	-	-	-	13.3	-
Cr	-	-	5.69	13.3	-	-
S	1.65	-	-	-	-	0.72

3.4 Vibrational FT-IR assignments

Fig. 6 displays the IR spectrum of $(C_6H_9N_2)_3[Cr(SCN)_6].H_2O$. Three characteristic vibrations can prove the presence of the thiocyanate ligand and its binding mode to the Cr(III) ion center for the formation of the anionic complex $[Cr(NCS)_6]$. The strong band at 2079 cm^{-1} can be assigned to the stretching vibration of the carbon-nitrogen triple bond of thiocyanic ligand. The weak band at 840 cm^{-1} can be attributed to C-S bond stretching vibration. The weak band at 490 cm^{-1} can be ascribed to the bending vibration of N–C-S. This vibration assignments of thiocyanate indicates the binding of thiocyanate ligand to Cr(III) center via its N-terminal atom. The assignment of these bands to thiocyanate vibrations and the determination of its coordination mode are based on

previously reported results **[53-57].** The spectrum shows also characteristic vibrations for 2-Amino-6-Methyl piridinium. The broad bands in the range 3600 - 2300 cm^{-1} correspond to the stretching vibrations of the organic and hydroxyl groups ν(N–H) and ν(C–H). The band at 1504 cm^{-1} corresponds to ν(C = C) stretching vibrations. The band at 1450 cm^{-1} can be assigned to the CH_2 deformation. The bands at 1244 and 1180 cm^{-1} can be attributed to the ring deformation. The weak bands at 1166 and 1021 cm^{-1} can be assigned to the CH_2 twisting. The weak band at 870 cm^{-1} can be attributed to the ring deformation **[58].**

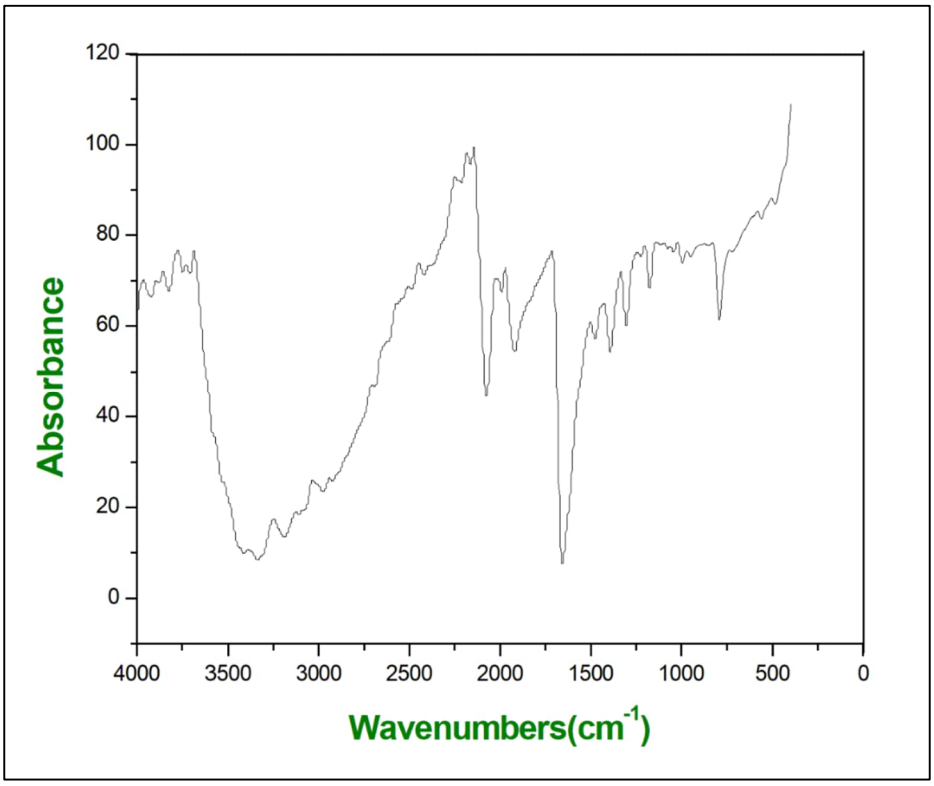

Fig. 6: Infrared absorption spectra of $(C_6H_9N_2)_3[Cr(SCN)_6].H_2O$.

3.5 Solid state UV–Visible absorption

The luminescence properties have been tested for the solid states of $(C_6H_9N_2)_3[Cr(SCN)_6].H_2O$ at room temperature, in the region 200–800 nm. As depicted **Fig.7**, the compound shows different luminescence behaviors; the two characteristic bonds at 558 nm (17922 cm^{-1}) and 417 nm (23980 cm^{-1}) are generated to d→d transitions for the Cr^{3+}. The calculation of Eg revealed that compound has a semiconductor behavior with a band value Eg = 3.19 eV **[59].** This behavior is probably due to the interactions in the molecular solid, to the charge transfer between the central metals and their coordinated ligands, and especially due to the presence of the thiocyanate anions that may affect the emission **[60].**

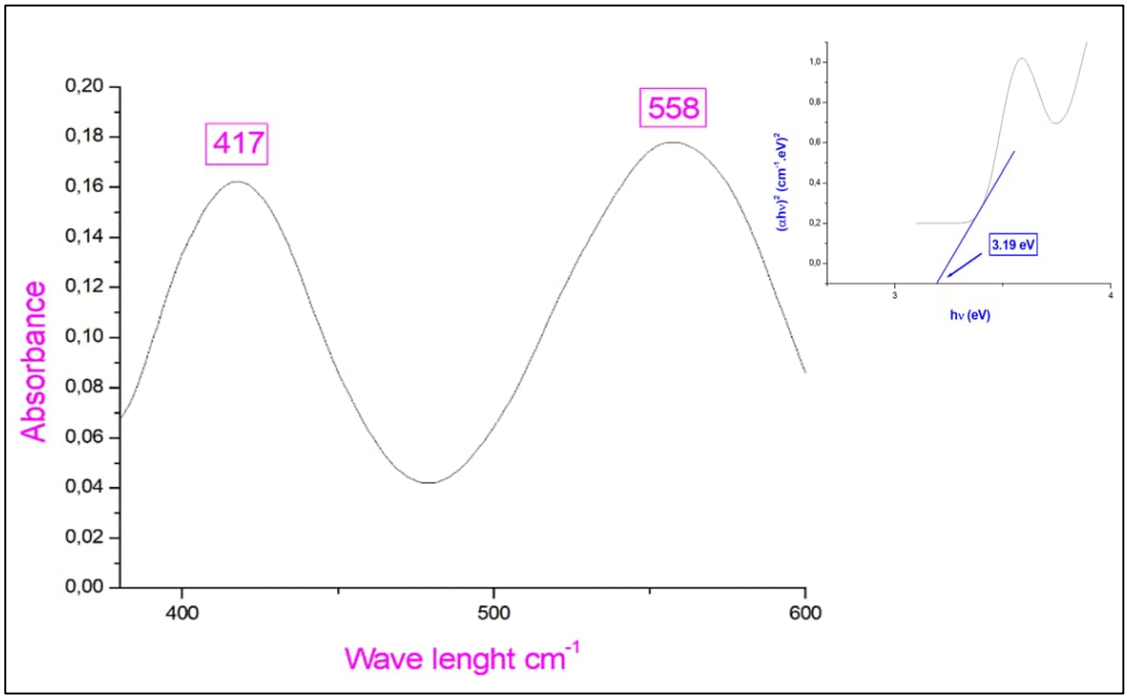

Fig. 7: Solid state UV–Vis spectrum of $(C_6H_9N_2)_3[Cr(SCN)_6].H_2O$.

3.5 Fluorescence

Fluorescence property of the obtained material have been determined in solid state at room temperature, by choosing the excitation wavelength at λ_{ex}= 433 nm, resulting in the emission spectrum illustrated in **Fig.8,** which gives for $(C_6H_9N_2)_3$ $[Cr(SCN)_6]\cdot H_2O$ it gives a spectrum having four bonds, the first at 372 nm which shows that this luminescence is at the origin of an intra-ligand transition (π -π*) of the cycle of the cation entity, the bonds at 404-438 nm corresponds to group transitions of (n -π*) belongs to the (C = S). the latest bond at 488 nm corresponds to the transition (d – d) of the Cr entity. The emission of synthetized compound was measured in front-face arrangement to the solid sample holder. The quantum yields in solution and in film were determined according to the relation**:**

$$\Phi_F = \Phi_F^S \frac{\int_0^\infty I^F(V)dV}{\int_0^\infty I_F^S(V)dV} \frac{1-10^{-A^S}}{1-10^{-A}} \quad (6)$$

where Φ_F^S is the quantum yield of standard, integrals $\int_0^\infty I^F(V)$ and $\int_0^\infty I_F^S(V)$ are the areas under curves of the probe and standard, while I^F(v) and I_F^S (v) is the intensity of fluorescence of probe and standard as function of number of waves, respectively, and A and A^S are absorptions of the probe and standard. As a result, the fluorescence quantum yield is Φ_F = 0.72 for $[(C_6H_9N_2)_3Cr(SCN)_6]\cdot H_2O$. The compounds are relatively high luminescent **[61].**

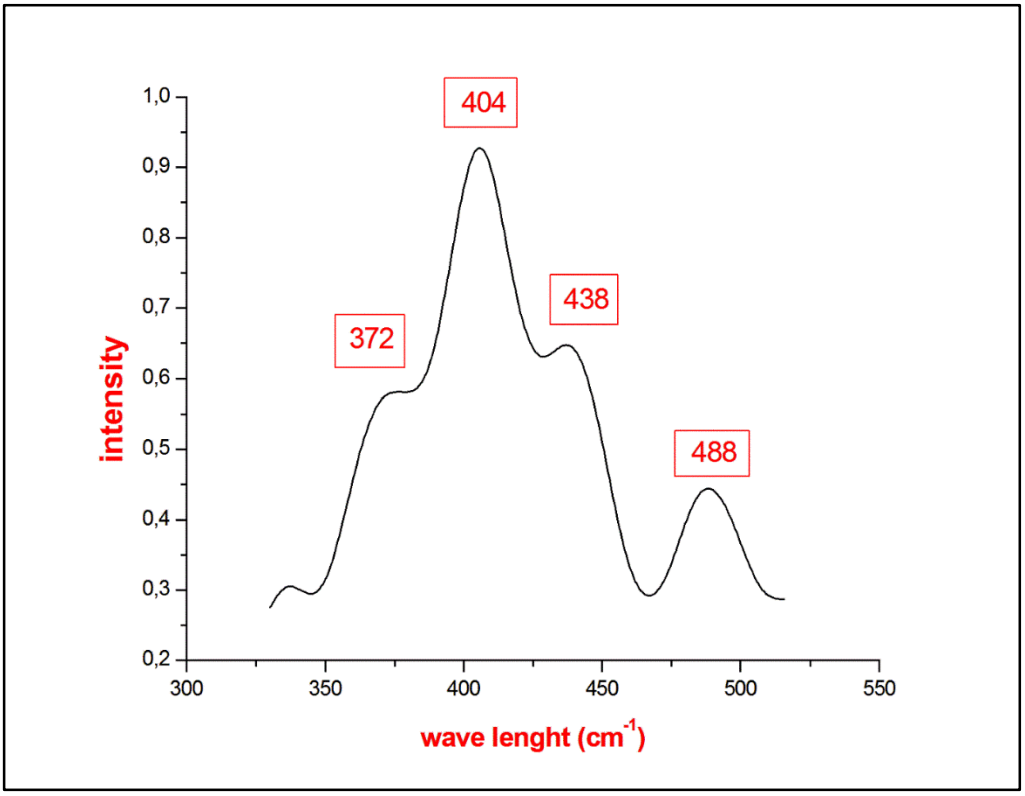

Fig. 8: Luminescence spectrum of the title compound.

3.6 Thermal studies

In metallurgy and materials science, annealing is a heat treatment that alters the physical and sometimes chemical properties of a material to increase its ductility and reduce its hardness, making it more workable. It involves heating a material above its recrystallization temperature, maintaining a suitable temperature for an appropriate amount of time and then cooling. The thermoanalytical data for $(C_6H_9N_2)_3$ $[Cr(SCN)_6].H_2O$ are given in **Table S3**. The combined DTA and DTG of the titled compound in dynamic air atmosphere, with heating rate of 5°C min^{-1}, are shown in **Fig. 9**. Four well defined steps can clearly be observed, in the ATD and DTG curves. The first peak at 363 K is associated with the endothermic loss of water accompanied by 5.025 % mass loss. This step is common to all the complexes and is similar to the dehydration of many other complexes with water of crystallization **[62].** The second step at 463 K belongs to the phase transition and its confirmed by dielectric study. An interesting observation in the thermal behavior

of $(C_6H_9N_2)_3$ $[Cr(SCN)_6].H_2O$ is the loss of the amine C-N groups from the equatorial ligand at 513 K . During this endothermic process, the mass loss in this step is 13.675 % and it can be attributed to successive decomposition of the titled complex. This endothermic step take place when the intermolecular N.H···S hydrogen bonding breaks apart in the deamination process and one of the three amines N-H groups per complex molecule is no longer engaged in hydrogen bonding. The mass loss in this step is 3.35 % and during this process the SO group, free from hydrogen bonding, is oxidized to SO_2 at 573 k. An expressive exothermic peak shown on the DTA curve at 623 k at the latest step is explained by an oxidation of the metal after the total decomposition of the sample, this step leads to obtain the CrO entity which is confirmed by FTIR analysis (**fig. S7**).

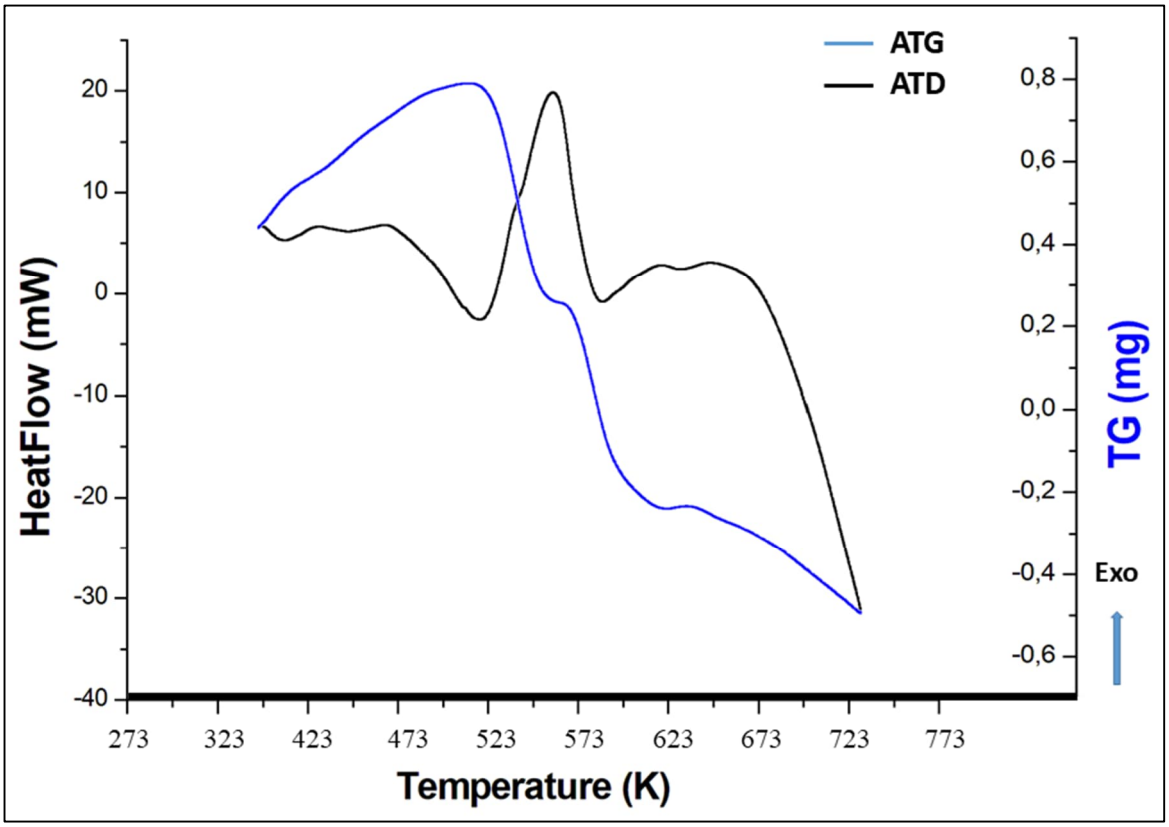

Fig. 9: ATD/ ATG thermograms of $(C_6H_9N_2)_3$ $[Cr(SCN)_6].H_2O$.

3.7 Electronic properties

3.7.1 HOMO-LUMO analysis

The frontier electron density is employed for anticipating the most reactive position in electron systems and also for explaining various forms of reaction in conjugated systems **[63-64].** Molecular orbitals and their features, such as energy, are highly helpful in the development of medications. Frontier molecular orbitals are defined as the highest occupied molecular orbitals (HOMOs) and lowest unoccupied molecular orbitals (LUMOs) (FMOs). Here, the border molecular orbitals of the investigated molecule were examined using the levels of theory B3LYP, PBE0, and ωB97XD/GEN. This was examined to consider the DFT approaches that, in terms of accuracy in reactivity and stability, more clearly define the biological potentials of the investigated molecule. However, the optical and electric properties, as well as quantum chemistry and UV-VIS spectra, are significantly influenced by the FMOs. The ability to give an electron is represented by the HOMO, and the ability to accept an electron is represented by the LUMO. Thus, the kinetic stability, chemical reactivity, optical polarizability, and chemical hardness-softness of a molecule are all determined by the energy gap between HOMO and LUMO, which are respectively related with ionization potential (IP) and electron affinity (EA). The HOMO-LUMO energy gap will be used to assess the energetic behavior of the molecule mentioned in the title. At the GEN/B3LYP level of theory, the computed energy values for E_{HOMO} and E_{LUMO} are 5.878 eV and 4.680 eV, respectively. The predicted energy difference between the HOMO and LUMO is 1.197 eV. On the other hand, ωB97XD/GEN clearly elucidate that the high E_{HOMO}-E_{LUMO} values of 7.701 eV and 3.129 eV, respectively, indicate a greater energy gap of 4.572 eV. However, this is because of the dispersion correction that the aforementioned approach possesses, which better explains adsorption investigations. The least energy difference of 0.218 eV resulting from the E_{HOMO} and E_{LUMO} values of 5.007 eV and 4.789 eV, respectively, was calculated using PBE0/GEN, which is interestingly stated by numerous literatures to account for substantial biological relevance. This further explains the eventual charge transfer interaction that occurs within the molecule and how it affects the molecule's biological function. As a result, the substantial stabilizing of the LUMO brought on by the electron-acceptor group's strong electron-acceptor ability is essentially what causes the reduction in the HOMO LUMO energy gap. **Figure 10** shows the 3D plots of the examined molecule's HOMO-LUMO, density of state (DOS), and respective energy gap computed at the B3LYP/GEN, PBE0/GEN, and ωB97XD/GEN Levels. As can be observed, the overlap of orbital loops on the HOMO and LUMO supports the existence of hydrogen bonding that is helped by resonance. The positive phase, which depicts the site

giving electrons, is red, while the negative phase, which depicts the site acquiring electrons, is blue. Several novel chemical reactivity descriptors have been developed to better comprehend certain pharmacological disciplines, such as drug design and potential eco-toxicological properties of the drug molecules. By computing the chemical potential (μ), global hardness (η), global softness (σ), electrophilicity (ω), and electro negativity (v), as indicated in **table S4**, conceptual DFT based descriptors have greatly aided in understanding the structure of the molecules and their reactivity. The ability of an electrophile to absorb extra electronic charge as well as the system's resistance to exchanging electronic charge with the environment are both included in the concept of electrophilicity. It was calculated to generate 8.342 eV, 1.306 eV, and 33.513 eV for B3LYP, PBE0, and ωB97XD, respectively, and is a better description of global chemical reactivity since it comprises data on both electron transport (chemical potential) and stability (hardness).

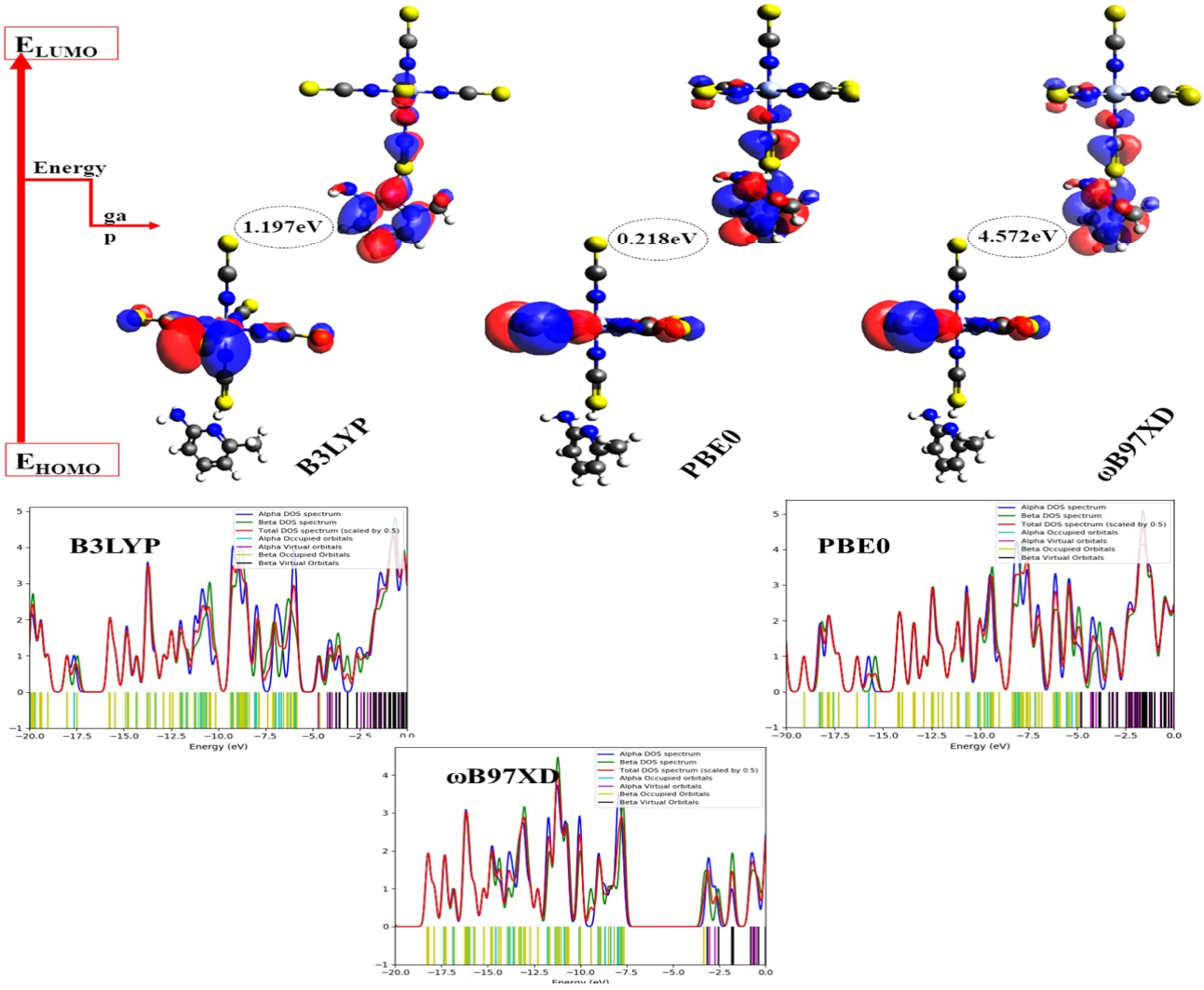

Fig.10: Plot illustrating the HOMO-LUMO analysis in line with density of state Spectrum

3.7.2 Natural bond orbital analysis

To investigate the electron density delocalization, charge transfer, and hyper-conjugative effects is natural bond orbital analysis **[65].** The donor-acceptor interaction that stabilizes molecular systems is reflected in the delocalization of electron density between filled (occupied Lewis's type) and unoccupied (non-Lewis) NBOs. Here, we take into account the second-order perturbation energy (E^2) value of the Fock matrix, which correlates to the energy exerted as a result of charge transfer between the donor I and acceptor (j) orbitals **[66].** The highest E^2 value indicates a higher donating ability from the donor to the acceptor and a greater perturbation energy/extent of conjugation of the entire system, and is used as a basis for investigation and understanding the strength of the interaction. In order to identify the stabilizing energy of every potential contact, which may be quantitatively described in terms of the second order perturbation interaction energy, this further consideration of charge transfers between non-covalent bonding and anti-bonding interaction is made **[67].** To better understand the intra- and intermolecular hybridization and the delocalization of electron density within the molecule, the stabilization energy E^2 associated with the delocalization of electron between the filled I and vacant orbital (j) of the compound was computed using the B3LYP/GEN, PBE0/GEN, and WB97XD/GEN level of theory. The output of the extracted second order perturbation theory analysis is calculated in **table S5**, and equation 2's mathematical derivation of the E2 value is provided.

$$\mathbf{E^{(2)}} = -n_{\sigma} \frac{(\sigma|\ \mathbf{F}|\ \sigma)^2}{\varepsilon\sigma' - \varepsilon\sigma} = -n\sigma \frac{F^2 \mathbf{IJ}}{\Delta \mathbf{E}} \qquad \mathbf{(7)}$$

ωB97XD/GEN revealed relatively very weak stabilization energies thus accounting for the donor to acceptor in the manner of strength arranged as thus; π C5 - N10 → π* C3 - C4 > π C3 - C4 → π* C 5 - N10 >π C5 - N10 → π* C1 - C2 > π C5 - N10 → π* C1 - C2 with respective perturbation energies of 35.86 kcal/mol, 33.94 kcal/mol, 22.13 kcal/, and 17.09 kcal/mol. On the other hand, B3LYP was examined to calculate significant sum perturbation energy of 107.47 at the transition of π→ π* this was expressed from the donor to acceptor arranged in the order of stronger intramolecular interaction of π C1 - C2 → π*C3 - C4 > π C1 - N10 → π*C4 - C5 > π C4 - C5 > π*C2 - C3 with calculated energies of 84.91 kcal/mol, 12.00 kcal/mol and 10.56 kcal/mol respectively. Whereas the π*→ π* (pi antibonding) transition was reported to predict weak intra and intermolecular interactions with a sum perturbation energy of 63.65 kcal/mol this is expressed in the manner as thus; π*C1 - N10 → π*C2 - C3 > π*C2 - C3 → π*C1 - N10 > π*C1 - N10 → π*C4 - C5 with generated stabilization energy of 28.70 kcal/mol, 20.39 kcal/mol and 14.56 kcal/mol

respectively. Fascinatingly, PBE0 yet calculated the highest sum stabilization energy of 143.28 at the π→ π* transition, hence agreeing with the energy gap as earlier discussed. This however evaluates the energetic behavior of the title compound, further implying that the method demonstrates the bioactivity from intra-molecular charge transfer as arranged as thus; π C1 - C2 → π*C3 - C4 > π C5 - N 10 → π*C3 - C4 > π C 5 - N 10 → π*C1 - C2 > π C3 - C4→ π*C5 - N10 with perturbation energies of 84.91 kcal/mol, 27.47 kcal/mol, 16.52 kcal/mol, 14.38 kcal/mol respectively.

3.7.3 Molecular Electrostatic Potential (MESP) and Natural Population Analysis (NPA)

The examination of MEPs in medication design is a potential application to deduce important finding from the studied compound. Molecular electrostatic potential (MESP) is a diagram of electrostatic potential over molecules with constant electron densities **[68-69]**. The key feature of MESP is the simultaneous display of molecular size, shape, and positive, negative, and neutral electrostatic potential regions in terms of a color grading scheme. This feature is extremely helpful in identifying the most likely binding receptor site as well as the molecular size and shape. In **figure 11(a)** the MESP plots of the studied molecule are shown. In a color grading system, the most electropositive, or electron-poor, region is represented by blue, while the most electronegative, or electron-rich, center is represented by red. The locations with zero electrostatic potential are represented by green. red < orange < yellow < green < blue are the colors in ascending order of electrical potential. The target molecule has an electric potential between -0.221 e 2 and 0.221 e. Around Cr, the highest electronegative potential zone may be noticed, and it is indicated by the color red. This is where electrophilic reactivity may occur. The band of very pale red color seen surrounding the nitrogen and sulfur represents the potential for an axial attack on this location. Hydrogen atoms, which constitute the greatest electropositive potential areas, have taken on a blue hue. It is one of the potential locations for a nucleophilic reaction.

The MEP is typically more of a qualitative than a quantitative instrument, and for establishing a correlation with pharmacological activity, the position of the extreme MEP values is more significant than the MEP values themselves. Because of this, it is not essential to generate the MEP using extremely complex techniques; correct atomic charges from a Mulliken population analysis as shown in **figure 11(b) and table S6** are adequate for such a calculation. Calculations can be done on the molecule's most stable form when there are electronic or conformational issues, which is consistent with the need that the MEP be taken into account in the reaction's recognition stage. Although a conformational fit may be created in the last stage of the reaction, in which case it is not possible to define the MEP extreme value positions for the corresponding conformation, the MEP can also be related to the stability of the complex formed between

the title compound and its receptor. The highly electronegative state of Cr in Fig.11 a and b suggests that it is full of electrons and would effectively serve as an electron donor in the molecule.

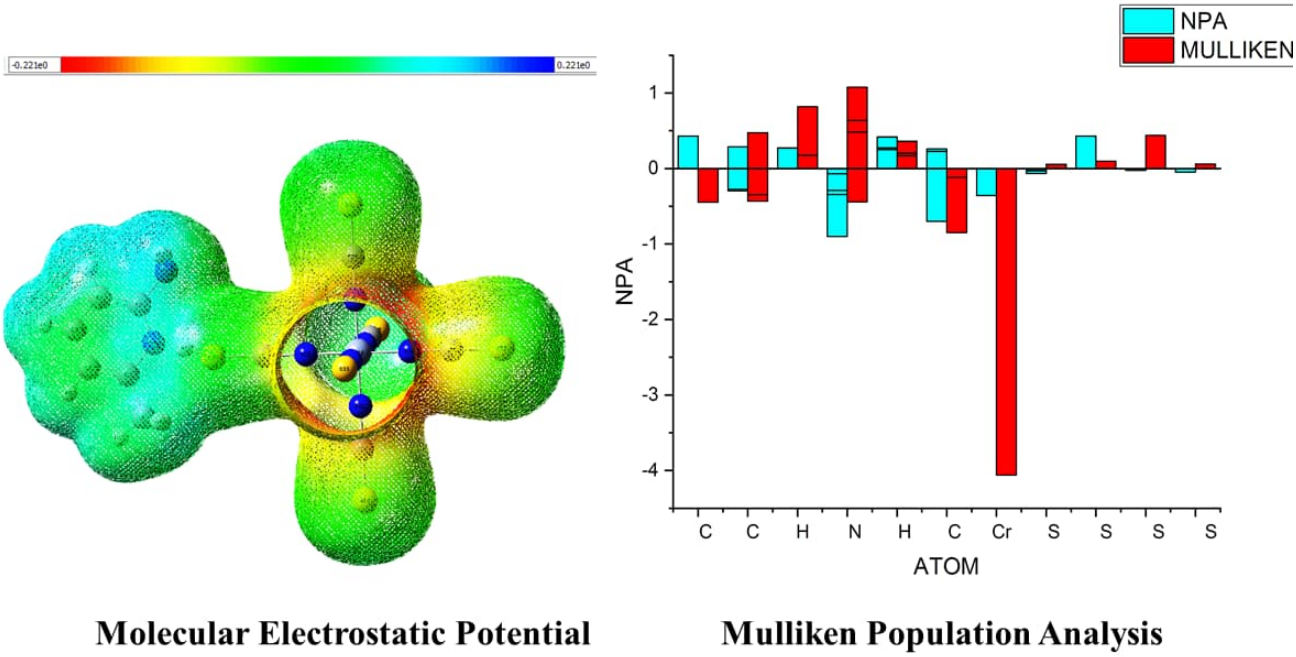

Fig.11a Analysis of the molecular electrostatic potential **Fig.11b** Plot of the Mulliken population analysis

3.8. Antioxidant activities

The different concentrations of the 70% ethanolic extract (0; 2.5; 5; 8; 11; 13.85 µg / ml) showed antioxidant activities in a dose-dependent manner 0, 3.49, 4.12, 5.8, 7.1 8.51% inhibition. In **Fig. S8**, it is shown that the percentage inhibition of the free radical DPPH (2,2-diphenyl-1-picrylhydrazyl) has the same pattern for the extract used. However, it has been observed that the percentage inhibition increases with the concentration of the 70% ethanolic extract as shown in **table S7** of the supporting information, it is generally lower when compared to that of the synthetic antioxidant DPPH which shows a higher antioxidant activity of the inhibition percentage **Fig. S8.**

The study of the antioxidant activity of the extract from Stevia rebaudiana using the DPPH free radical scavenging method showed that the 70% ethanolic extract has significant antioxidant activity. However, this activity remains significantly lower than that of DPPH, but it is a crude extract containing a large number of different compounds. It is therefore very likely that it contains compounds which, once purified, may exhibit activity comparable to that of DPPH. The antioxidant capacity is expressed in Trolox equivalent (TEAC) which gives a value of EC50 = 18.22 ± 0.05 µg / ml; it corresponds to the concentration of Trolox which gives a value of EC50 Trolox = 21.642 µM, having the same activity as the substance to be tested at one concentration. The result is given in µM of Trolox equivalent per g of product with a value of 1.219 µmoles Trolox / mg of extract. Scavenger effect of the DPPH radical The anti-free radical activity of the various extracts **[70]** was evaluated by their inhibitory activity on a methanolic solution of DPPH, measured at 517 nm. We interpret this phenomenon by the transfer of the single electrons which are located in the external orbital of the DPPH, and after reaching a given concentration, the antioxidant will react completely with the radical, and when we increase the concentration, the antioxidant activity of the compound could be explained by the presence of an important capacity to act as donors of hydrogen or electron atoms, hence the reductive transformation of DPPH • into DPPH-H, and consequently the formation of the Yellow coloration was attributed to the presence of numerous bioactive molecules which is accompanied by the saturation of the electronic layers of the radical.

3.9 Molecular docking analysis

In this study, virtual screening via molecular docking was performed on the synthesized complex docked with 4CIA to further understand the biological activities and applications as a potential cardiovascular disease drug candidate [**71, 72**]. The obtained result was further compared with a commercial drug clopidogrel with access code (DB00758). Clopidogrel has recently been reported to have numerous side effect including: nosebleed, stomach pain and excessive tiredness hence the reason for the developing a novel cardiovascular disease drug. The result of the binding affinity is presented in **table S8**, from the table it is observed that the interaction between the complex and the selected protein had the binding affinity of −4.6(kcal/mol). Whereas, clop@4CIA calculated -6.8 kcal/mol as its potential binding affinity. From the obtained results it is worth mentioning that the interaction between the complex and the target protein receptor (4CIA)

elucidated strong binding potential. Also, it is very clear to point out that target protein had great interaction with the drug (clopidogrel). Furthermore, the synthesized complex interacted with the protein revealed the highest conventional hydrogen bond from the 9-pose generated. F**igure 12 explains the** four hydrogen bonds established as amino-acid residues with their respective bond distance (A; ASN 30, A: ALA30, UNKO:H and UNKO:H). Meanwhile the standard drug was examined not to generate any hydrogen bond, implying the occurrence of a very weak inhibitory potential compared to that of the studied complex. Thus, the head complex therefore can serve as an alternative drug candidate for the treatment of cardiovascular disease.

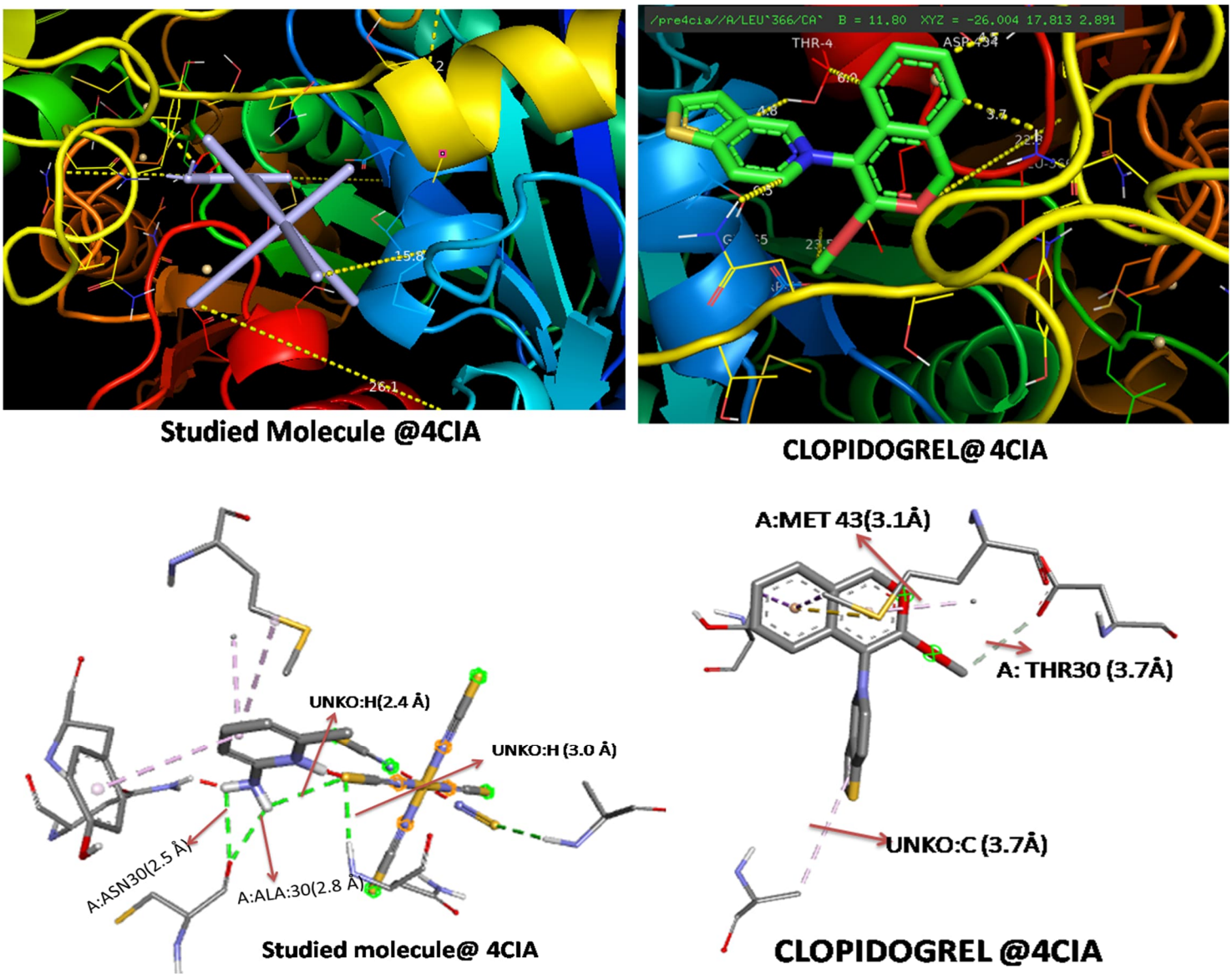

Fig.12 3D Pymol and Biovia discovery studio visualization of the target receptor(4CIA) with the studied compound and the conventional drug (clopidogrel)

4.0 Conclusions

The synthesis and characterization of novel coordination compound *[($C_6H_9N_2$)$_3$Cr(SCN)$_6$]·H_2O]*, has been described and In the Chrom-complex; the metal center was found to be hexacoordinated with six NCS entities establishing an octahedral geometry.

The intermolecular cohesion is ensured by O–H…S, N–H…O and N–H…S hydrogen bonds which enhance the robustness of the crystal. In addition, the optical properties were investigated by FT-IR absorption measurement add to solid state Ultra-violet measurements. A thermal study by differential thermal analysis (DTA) and thermal gravimetric analysis (TGA) which highlights the stability and the decomposition ranges.

Hirshfeld surface analysis shows the main interactions responsible for molecular packing in complex structure. The HOMO-LUMO and quantum descriptors helps to study the charge transfer and chemical reactivity, as a result, the reduction in the HOMO LUMO energy gap is primarily due to the substantial stabilizing of the LUMO caused by the electron-acceptor group's strong electron-acceptor ability.

The antioxidant assay proves a high biological behavior of the titled compound. The biological activity of the compound was cross validated by molecular docking, the enzyme revealed several key active site residues to form short distance hydrophilic and hydrophobic contacts with the compound, these results confirm that the titled compound may be used as a substitute medication candidate for the treatment of cardiovascular disease. These results are a good indication that the nature of the metal used has an important effect on the coordination compounds characterization.

Appendix A. Supplementary material

A CCDC Deposition Number 2061181 contain the supplementary crystallographic data for. This data can be obtained free of charge via http://www.ccdc.cam.ac.uk/conts/retrieving.html, or from

the Cambridge Crystallographic Data Center, 12 Union Road, Cambridge CB2 1EZ, UK; fax: (+44) 1223-336-033; or email: deposit@ccdc.cam.ac.uk.

References

[1] Plakatouras, J. C., Perlepes, S. P., Mentzafos, D., Terzis, A., Bakas, T., & Papaefthymiou, V. Polyhedron, (1992), 11(20), 2657–2672.

[2] Hong-Li Jia,a Ming-Jun Jia,b Guang-Hua Li,a Yan-Ning Wang,a Jie-Hui Yu a and Ji-Qing Xu, This journal is The Royal Society of Chemistry 2013, Dalton Trans., (2013), 42, 6429–6439.

[3] Mohd. Muddassir and You Song Crystals, (2020), 10, 87.

[4] A. A. Bagabas , M. Alsawalha , M. Sohail , S. Alhoshan, R. Arasheed ; Heliyon 5 (2019) e01139.

[5] Hai-Ying Biea, Jie-Hui Yua, Ji-Qing Xua, Jing Lua, Yong Lia, Xiao-Bing Cuia,b, Xiao Zhanga, Ying-Hua Suna, Ling-Yun Panc Journal of Molecular Structure, (2003). 7(1),51-54.

[6] Marta Pockaj, Nives Kitanovski, Boris Ceh and Romana Cerc-Korosec . Acta Chim. Slov. (2017), 64, 342–348.

[7] Vincent, J. B. The Biochemistry of Chromium. The Journal of Nutrition, (2000). 130(4), 715–718.

[8] Ellis, A. S. Chromium Isotopes and the Fate of Hexavalent Chromium in the Environment. Science, (2002). 295(5562), 2060–2062.

[9] Pavol Hrdlovi, Jozef Kollár, Štefan Chmela, Journal of Photochemistry and Photobiology A: Chemistry 163 (2004) 289–296.

[10] A. Volkov, P. Coppens. J. Comput. Chem. (2004) 921-934.

[11] Ronald T. Pflaum and Lester C. Howick, Anal. Chem, (1956), Vol. 78, 4862.

[12] N. Saha, S.K. Kar. J. Inorg. Nucl. Chem., (1977).39, 195.

[13] N. Adhikari, S. Chowdhury, R.J. Butcher, N. Saha. Polyhedron, (1999). 18, 1323.

[14] S. Develay, O. Blackburn, A.L. Thompson, J.A.G. Williams. Inorg. Chem., (2008). 47, 11129.

[15] D.J.A. Chaturvedi, R.K. Upadhayay. J. Chem., (2011). 8, 113.

[16] J. Reedijk, in: G. Wilkinson, R.D. Gillard, J.A. McCleaverty (Eds.), Comprehensive Coordination Chemistry, Vol. 2, Pergamon, Oxford (1987).

[17] T.B. Thederahn, M.D. Kuwabara, T.A. Larsen, D.S. Sigman. J. Am. Chem. Soc., (1989). 111, 4941.

[18] S. Singh, N. K. Relhan, R. K. Kotnala, and K. C. Verma (2012). Indian J. Pure Appl. Phys. 50, 739.

[19] C. Santini, M. Pellei, V. Gandin, M. Porchia, F. Tisato, C. Marzano. Chem. Rev., (2014). 114, 815.

[20] G. Sheldrick, Acta Crystallographica. Sect. A (2015). 71, 3.

[21] Farrugia LJ, Journal Application Crystallography (1999), 32:837–838.

[22] G. Vezzalini, S. Quartieri, A. Sani, D. Levy,A. Galarneau, F. Di Renzo, F. Fajula, J. Vedrine (Eds.), Studies in Surface Sciences and Catalysis, 2001, p. 135.

[23] O. Ferro, S. Quartieri, G. Vezzalini, E. Fois, A. Gamba, G. Tabacchi, Am. Mineral. 87 (2002) 1415–1425.

[24] Louli, V., Ragoussis, N., & Magoulas, K. Bioresource Technology, (2004). 92(2), 201–208.

[25] S.K. Wolff, S.D.J. Greenwood, J.J. McKinnon, D. Jayatilaka, M.A. Spackman, CrystalExplorer 3.1, University of Western Australia, Perth, Australia, 2013.

[26] M. J. Frisch, G. W. Trucks, H. B. Schlegel, G. E. Scuseria, M. A. Robb, J. R. Cheeseman, G. Scalmani, V. Barone, G. A. Petersson, H. Nakatsuji, X. Li, M. Caricato, A. V. Marenich, J. Bloino, B. G. Janesko, R. Gomperts, B. Mennucci, H. P. Hratchian, J. V. Ortiz, A. F. Izmaylov, J. L. Sonnenberg, D. Williams-Young, F. Ding, F. Lipparini, F. Egidi, J. Goings, B. Peng, A. Petrone, T. Henderson, D. Ranasinghe, V. G. Zakrzewski, J. Gao, N. Rega, G. Zheng, W. Liang, M. Hada, M. Ehara, K. Toyota, R. Fukuda, J. Hasegawa,

M. Ishida, T. Nakajima, Y. Honda, O. Kitao, H. Nakai, T. Vreven, K. Throssell, J. A. Montgomery, Jr., J. E. Peralta, F. Ogliaro, M. J. Bearpark, J. J. Heyd, E. N. Brothers, K. N. Kudin, V. N. Staroverov, T. A. Keith, R. Kobayashi, J. Normand, K. Raghavachari, A. P. Rendell, J. C. Burant, S. S. Iyengar, J. Tomasi, M. Cossi, J. M. Millam, M. Klene, C. Adamo, R. Cammi, J. W. Ochterski, R. L. Martin, K. Morokuma, O. Farkas, J. B. Foresman, and D. J. Fox, Gaussian, Inc., Wallingford CT, 2016.

[27] R. Dennington., T.A. Keith., & J. M. Millam., GaussView 6.0. 16.

[28] Liu, Z., Lu, T., & Chen, Q. (2020). *165*, 461-467.

[29] E. V. Cherkasova, N. V. Pervukhinab, N. V. Kuratievab, and T. G. Cherkasova, Inorg. Chem, (2019), 64, 329–334.

[30] H. A Schreuder., A. Liesum, K. Kroll., B. Böhnisch., C. Buning, S. Ruf., &, T. Sadowski (2014). Bio and Biophysical Res Comm, 445(2), 451-456.

[31] H.Q. Ye, Y.Y. Li, R.K. Huang, X.P. Liu, W.Q. Chen, J.R. Zhou, L.M. Yang, C.L. Ni, J.Struct. Chem. 55 (2014) 691–696.

[32] Einstein, F. W. B. Gilbert,M. Tuck, D. G. Acta Crystallogr., Sect. B. (1976), B32, 2234.

[33] W.Q. Chen, L.J. Su, X.Q. Cai, J.J. Yang, Y.L. Qian, X.P. Liu, L.M. Yang, J.R. Zhou,C.L. Ni, Synth. React. Inorg. Met. Org. Nano Met. Chem 44 (2014) 980–985.

[34] H.Q. Ye, L.J. Su, X.X. Chen, X. Liao, Q.T. Liu, X.Y. Wu, J.R. Zhou, L.M. Yang, C.L. Ni,Synth. Met. 199 (2015) 232–240.

[35] H.Q. Ye, J.L. Xie, J.Y. Yu, Q.T. Liu, S.L. Dai, W.Q. Huang, J.R. Zhou, L.M. Yang,C.L. Ni, Synth. Met. 197 (2014) 99–104.

[36] H.Q. Ye, Y.Y. Li, R.K. Huang, X.P. Liu, W.Q. Chen, J.R. Zhou, L.M. Yang, C.L. Ni, J.Struct. Chem. 55 (2014) 691–696.

[37] Makhlouf, J., El Bakri, Y., Valkonen, A., Saravanan, K., Ahmad, S., & Smirani, W. Polyhedron, (2022). 115937.

[38] Z. Zhang, J. Xu, S. Yan, Y. Chen, Y. Wang, Z. Chen, C.L. Ni, Crystals (2017).92–105.

[39] Steiner T, Angew Chem Int Ed (2002). 41:48–76.

[40] I.D. Olekseyuk, O.V. Parasyuk, O. Husak, L.V. Piskach, S.V. Volkov, V.I. Pekhnyo,

J. Alloys Compds. (2005). 402.186.

[41] M. Leo´n, J.M. Merino, J.L. de Vidales, J. Mater. Sci. (1992) 27, 4495.

[42] J.J. McKinnon, M.A. Spackman, A.S. Mitchell, Acta Crystallogr. (2004), B 60, 627e668.

[43] M.A. Spackman, P.G. Byrom, Chemical Physics. Lett. (1997) 267, 215e220.

[44] S. Partitioning, C. Density, Spatial Partitioning of Charge Density, (1977) 198–201.

[45] D.P. Mackinnon, C.M. Lockwood, (2010) 37–41.

[46] Jelsch, C., Ejsmont, K., & Huder, L. (2014). 1(2), 119–128.

[47] Defersha, M. B., & Melesse, A. M. (2012). 90, 47–52.

[48] E.M. Rakhmanko, Y.V. Matveichuk, V.V. Yasinetskii, J. Anal. Chem. (2015) 70, 178–185.

[49] H.T. Cai, Q.T. Liu, H.Q. Ye, L.J. Su, X.X. Zheng, J.N. Li, S.H. Ou, J.R. Zhou,L.M. Yang, C.L. Ni, Spectrochim. Acta A Mol. Biomol. Spectrosc. (2015). 142,239–245.

[50] G.M. Ionita, G. Ilie, C. Angel, F. Dan, D.K. Smith, V. Chechik, Langmuir (2013) 29,

9173–9178.

[51] S.J. Osborne, S. Wellens, C. Ward, S. Felton, R.M. Bowman, K.B. Binnemans,M. Swad_zba-Kwa_sny, H.Q.N. Gunaratne, P. Nockemann, Dalton Trans (2015) 44,11286–11289.

[52] A.A. Bagabas, M. Alsawalha, M. Sohail, S. Alhoshan, R. Arasheed, Heliyon (2019), 5,e01139.

[53] Makhlouf, J., Valkonen, A., and Smirani Sta, W. Journal of Coordination Chemistry, (2022). 1-22.

[54] H.T. Cai, Q.T. Liu, H.Q. Ye, L.J. Su, X.X. Zheng, J.N. Li, S.H. Ou, J.R. Zhou, L.M. Yang, C.L. Ni, Spectrochim. Acta, Part A: Mol. Biomol. Spectrosc. (2015), 142 ,239.

[55] Pavol Hrdlovi, Jozef Kollár, Štefan Chmela, Journal of Photochemistry and Photobiology A: Chemistry (2004),163, 289–296.

[56] D. Czakis-Sulikowska and J. Ka³uzna, J. Thermal Anal., (1996), 47,1763.

[57] H. Khemakhem, T. Mhiri, and A. Daoud, Solid State Ionics (1999). 117, 337.

[58] A. Nazir, M. M. Ahmad, and P. N. Kotru J. Cryst. Growth (2015). 412, 72.

[59] B. Rajagopal, A. V. Sharma, and M. V. Ramana Arch. Appl. Sci. Res. (2011). 3, 321.

[60] I. Lahbib, M. Rzaigui, and W. Smirani J. Mol. Struct. (2016).1120, 250.

[61] S. Singh, N. K. Relhan, R. K. Kotnala, and K. C. Verma Indian J. Pure Appl. Phys. (2012). 50, 739.

[62] K. Karoui, A. Ben Rhaiem, F. Hlel, M. Arous, and K. Guidara Mater. Chem. Phys. (2012). 133, 1.

[63] I. Benjamin., A. D. Udoikono., H. Louis., E. C. Agwamba., T. O. Unimuke., A. E. Owen., & A. S. Adeyinka (2022). 133298.

[64] E. A. Eno., H. Louis., P. Ekoja., I. Benjamin., S. A. Adalikwu., M. M. Orosun., ... & E. C. Agwamba (2022). *99*(7), 100532.

[65], E. A. Eno., J. I. Mbonu., H. Louis., F. S. Patrick-Inezi., T. E. Gber., T. O. Unimuke, ... & O. E. Offiong (2022). *99*(7), 100524.

[66] E. C. Agwamba, A. D. Udoikono., H. Louis., E. U. Udoh, Benjamin, I., Igbalagh, A. T., ... & Ushaka, U. B. (2022). 100076

[67] F. C. Asogwa., E. C. Agwamba., H. Louis., M. C. Muozie., I. Benjamin., T. E. Gber., ... & A. I. Ikeuba (2022). 100091.

[68] H. Louis., T. E. Gber., F. C. Asogwa., E. A. Eno., T. O. Unimuke., V. M. Bassey., &, B. I. Ita (2022). *278*, 125518.

[69] E. A. Eno., J. I. Mbonu., H. Louis., F. S. Patrick-Inezi., T. E. Gber., T. O. Unimuke ... & O. E. Offiong, (2022).

[70] J, Pokorny., N. Yanishlieva., M. Gordon. (2001). 72(5):145-71.

[71] A. Vidal-Limon., J. E. Aguilar-Toalá., & A. M. Liceaga. (2022). 70(4), 934-943.

[72] A. M. Omar., G. A. Mohamed & S. R. Ibrahim (2022). 8(2), 127.